Monthly Notices
of the
ROYAL ASTRONOMICAL SOCIETY

Mon. Not. R. Astron. Soc. **416,** 38–50 (2011) doi:10.1111/j.1365-2966.2011.18946.x

The effects of the interactions on the kinematics, stellar population and metallicity of AM 2322−821 with Gemini/GMOS

A. C. Krabbe,[1⋆] M. G. Pastoriza,[2] Cláudia Winge,[3] I. Rodrigues,[1] O. L. Dors[1] and D. L. Ferreiro[4]

[1]*Universidade do Vale do Paraíba, Av. Shishima Hifumi, 2911, Cep 12244-000, São José dos Campos, SP, Brazil*
[2]*Instituto de Física, Universidade Federal do Rio Grande do Sul, Av. Bento Gonçalves, 9500, Cep 91359-050, Porto Alegre, RS, Brazil*
[3]*Gemini Observatory, c/o AURA Inc., Casilla 603, La Serena, Chile*
[4]*IATE, Observatório Astronómico, Universidad Nacional de Córdoba, Laprida 854, 5000 Córdoba, Argentina*

Accepted 2011 April 19. Received 2011 March 28; in original form 2010 July 9

ABSTRACT

We present an observational study of the impacts of the interactions on the kinematics, stellar populations and oxygen abundances of the components of the galaxy pair AM 2322−821. A fairly symmetric rotation curve for the companion (AM 2322B) galaxy with a deprojected velocity amplitude of 110 km s^{-1} was obtained, and a dynamical mass of 1.1–1.3 × 10^{10} $M_{\odot}$ within a radius of 4 kpc was estimated using this deprojected velocity. Asymmetries in the radial velocity field were detected for the companion, very likely due to the interaction between the galaxies. The interaction between the main and companion galaxies was modelled using numerical *N*-body/hydrodynamical simulations, with the result indicating that the current stage of the system would be about 90 Myr after perigalacticon. The spatial variation in the distribution of the stellar population components in both galaxies was analysed using the stellar population synthesis code STARLIGHT. The companion galaxy is dominated by a very young ($t \leq 1 \times 10^8$ yr) population, with the fraction that this population is of the total flux at λ 5870 Å increasing outwards in the galaxy disc. On the other hand, the stellar population of AM 2322A is heterogeneous along the slit positions observed. Spatial profiles of oxygen abundance in the gaseous phase were obtained using the diagnostic diagram R_{23} = ([O II]λ 3727 +[O III] λ 4959 +[O III] λ 5007)/Hβ versus [O III]λ 5007/[O II]λ 3727 where we compared the observed values with the ones obtained from photoionization models. Such gradients of oxygen abundance are significantly flatter for this pair of galaxies than in typical isolated spiral galaxies. This metallicity distribution is interpreted as the gradients having been destroyed by interaction-induced gas flows from the outer parts to the centre of the galaxy.

Key words: galaxies: abundances – galaxies: general – galaxies: interactions – galaxies: kinematics and dynamics – galaxies: starburst – galaxies: stellar content.

1 INTRODUCTION

Galaxy interactions and merger events play an important role in the evolution and the stellar formation history of galaxies. Interacting/merging galaxies show enhanced star formation when compared with isolated objects, as indicated by various studies (Kennicutt et al. 1987; Sekiguchi & Wolstencroft 1992; Donzelli & Pastoriza 1997; Barton Gillespie, Geller & Kenyon 2003; Geller et al. 2006; Woods & Geller 2007). This enhancement has been found to be a function of the projected galaxy pair separation (e.g. Barton, Geller & Kenyon 2000; Lambas et al. 2003; Nikolic, Cullen & Alexander 2004) as well as to be stronger in low-mass than in high-mass galaxies (e.g. Woods & Geller 2007; Ellison et al. 2008).

The induced star formation associated with the gas motions created by the interaction is also expected to have an impact on the chemical state of the galaxies. As star formation enriches the interstellar medium via nucleosynthesis, inflows of metal-poor gas from the outer parts of the galaxy can decrease the metallicity in the inner regions and modify the radial abundance gradients across the spiral discs. In fact, studies have found that interacting galaxies do not follow the well-established correlation between luminosity and metallicity found in normal disc galaxies. The central regions of these galaxies are underabundant when compared to isolated galaxies of similar mass (Kewley, Geller & Barton 2006; Ellison et al. 2008; Michel-Dansac et al. 2008; Rupke, Veilleux & Baker 2008; Peeples, Pogge & Stanek 2009).

⋆E-mail: angela.krabbe@gmail.com

Shallower metallicity gradients have been found in barred galaxies and explained by the action of inward and outward radial flows of interstellar gas induced by the non-axisymmetric potential of bars (e.g. Sellwood & Wilkinson 1993; Friedli, Benz & Kennicutt 1994; Roy & Walsh 1997). *N*-body/smoothed particle hydrodynamics numerical simulations of equal-mass mergers, although they ignore the presence of ongoing star formation, predict that the radial metallicity gradients in disc galaxies flatten shortly after the first pericentre passage, due to the radial mixing of gas (Rupke, Kewley & Barnes 2010). Recently, Kewley et al. (2010) determined the metallicity gradients for eight galaxy pairs with a mass ratio near unity and showed that they were significantly shallower than those in isolated spiral galaxies. Furthermore, Krabbe et al. (2008) found for the interacting pair AM 2306−721 with a mass ratio of 2:1 that the disc of the main galaxy showed a clear radial metallicity gradient, while the secondary presented a relatively homogeneous oxygen abundance. These authors interpreted the absence of abundance gradient in the secondary galaxy in terms of mixing the low-metallicity gas from the outer parts with the metal-rich gas of the centre of the galaxy. Is this picture always reproduced in other minor mergers? This question was not addressed before by theoretical merger simulations and observations, except for the above study of AM 2306−721. Therefore, more observational studies of mergers with different mass ratios should provide useful insights to answer the above question. We have selected from Ferreiro & Pastoriza (2004) several systems to study the effects of the kinematics, stellar population and gradient abundances of the galaxies in minor mergers, where the first results of this programme were presented for AM 2306−721 (Krabbe et al. 2008).

This paper presents the results for the system AM 2322−821, which is morphologically very similar to AM 2306−721, but its mass ratio is much lower than that of AM 2306−721. AM 2322−821 is composed of an SA(r)c galaxy with disturbed arms (hereafter AM 2322A) in interaction with an irregular galaxy (hereafter AM 2322B). Both galaxies contain very luminous H II regions with Hα luminosity in the range of $2.53 \times 10^{39} < L(\mathrm{H}\alpha) < 1.45 \times 10^{41}\,\mathrm{erg\,s^{-1}}$ as estimated from Hα images, and a high star formation rate in the range of 0.02–1.15 $\mathrm{M_\odot\ yr^{-1}}$ (Ferreiro, Pastoriza & Rickes 2008).

The present paper is organized as follows. In Section 2, we summarize the observations and data reduction. The gas kinematics of each galaxy and the numerical *N*-body/hydrodynamical simulations of the interaction are presented in Sections 3 and 4, respectively. In Section 5, we present the stellar population synthesis. The metallicity analysis is presented in Section 6, and the conclusions are summarized in Section 7.

2 OBSERVATIONS AND DATA REDUCTION

Long-slit spectroscopic data were obtained on 2006 June 29/30, 2006 July 01/02 and 2008 July 27/28 with the Gemini Multi-Object Spectrograph at Gemini South, as a part of the poor-weather programmes GS-2006A-DD-6 and GS-2008A-Q-206. Spectra in the range of 3450–7130 Å were obtained with two settings with the B600 grating, and the 1-arcsec slit, keeping a compromise between spectral resolution (∼5.5 Å), spectral coverage and slit losses (due to the Image Quality = ANY constraint). The blue setting provided a wavelength coverage of 3450–6280 Å and the red setting of 4280–7130 Å at about the same spectral resolution. The frames were binned on-chip by 6 and 2 pixels in the spatial and spectral directions, respectively, resulting in a spatial scale of 0.288 arcsec $\mathrm{pixel^{-1}}$, and 0.9 Å $\mathrm{pixel^{-1}}$ dispersion.

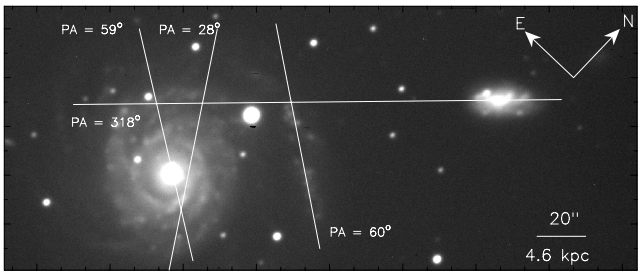

Figure 1. GMOS-S r'-band image of AM 2322−821 with the observed slit positions.

Spectra were taken at four different position angles in the sky, with the goal of observing the nucleus and the brightest regions of the galaxies, as well as one spiral arm that is away from the main galaxy. PA = 59° is in the slit position crossing the nucleus of AM 2322A; PA = 28° is cutting across the main body of the primary, but not across the nucleus [an offset of about 8 arcsec north-west (NW) from the nucleus]; the slit position at PA = 60° is located off the disc of the main component, along the NW spiral arm (located between the main and secondary component). The PA = 318° slit position is oriented along the main axis disc of the secondary component (AM 2322B) and also along the AM 2322A north-east (NE) spiral arm. Observations for PA = 60° were made only in the red spectra, and thus in this slit it was possible only to study the ionized gas kinematics but not their stellar population and the gas phase O/H abundance. Fig. 1 shows the four slit positions on the GMOS-S r' acquisition image.

The exposure time on each single frame was limited to 700 s to minimize the effects of cosmic rays, with multiple frames being obtained for each slit position to achieve a suitable signal. The slit positions are shown in Fig. 1, superimposed on the r'-band image of the pair. Table 1 gives the journal of observations. Conditions during both the runs were not photometric, with a thin cirrus and an image quality in the range of 0.5–2.0 arcsec (as measured from stars in the acquisition images taken just prior to the spectroscopic observations).

The spectroscopic data reduction was carried out using the GEMINI.GMOS package as well as generic IRAF tasks. We followed the standard procedure: (1) the data were bias subtracted and flat-fielded; (2) the wavelength calibration was established from the Cu–Ar arc frames with typical residuals of 0.2 Å and applied to the object frames; (3) the individual spectra of the same slit positions and wavelength range were averaged with cosmic ray rejection; (4) the object frames were sky subtracted interactively using the gsskysub task, which uses a background sample of off-object areas to fit a function to the specified rows, and this fit is then subtracted from the column of each spectrum; (5) the spectra were relative flux calibrated using observations of a flux standard star taken with the same

Table 1. Journal of observations.

Date (UT)	Exposure time (s)	PA (°)	Δλ (Å)
2006 June 29	3 × 600	318	4280–7130
2006 June 30	6 × 600	60	4280–7130
2006 July 01	2 × 600	28	4280–7130
2006 July 01	3 × 700	59	4280–7130
2006 July 01	3 × 600	318	4280–7130
2008 July 27	6 × 600	28	3450–6270
2008 July 27	6 × 600	59	3450–6270
2008 July 27	6 × 600	318	3450–6270

set-up as the science observations; (6) finally, one-dimensional spectra were extracted from the two-dimensional spectra by summing over six rows along the spatial direction. Each spectrum therefore comprises the flux contained in an aperture of $1 \times 1.73\,\mathrm{arcsec}^2$. Assuming a distance of 49.6 Mpc for the AM 2322−821 system barycentre (estimated from the radial velocities derived in Section 3 and the total masses of AM 2322A and AM 2322B, estimated in Section 4, and adopting $H_0 = 75\,\mathrm{km\,s^{-1}\,Mpc^{-1}}$), this aperture corresponds to a region of $241 \times 419\,\mathrm{pc}^2$ for AM 2322−821. The nominal centre of each slit was chosen to be the continuum peak at λ 5735 Å. The mismatch between the blue and red spectra for all the apertures extracted was lower than about 5 per cent over the spectral range where the two spectra overlapped. We decided not to co-add them.

3 IONIZED GAS KINEMATICS

The radial velocity was estimated from the strongest emission lines present in the spectra, namely Hβ λ4861, [O III] λ5007, Hα λ6563 and [N II] λ6584. The final radial velocity for each spectrum was obtained by averaging the individual measurements from the detected emission lines, and the errors were estimated from the standard deviation of the individual measurements around the mean.

The inclination of each galaxy with respect to the plane of the sky was computed as $\cos(i) = b/a$, where a and b are the minor and major semi-axes of the galaxy, respectively. The minor and major semi-axes as well as the position angle of the major axis of each galaxy were obtained from the acquisition images in the r' filter, using a simple isophotal fitting with the IRAF STSDAS.ELLIPSE task. The fitting results for the position angle of the major axis and the inclination as a function of the projected distance in arcseconds along the isophotal major axis are shown in Figs 2 and 3, for AM 2322A and AM 2322B, respectively.

For AM 2322B, the position angle of the major axis and the inclination of the galaxy are nearly constant up to a 5-arcsec radius. The resulting values for the disc inclination and position angle of the line of nodes are $i = 63^\circ$ and $\psi_0 = 318^\circ$, respectively. For AM 2322A, the position angle of the major axis and the inclination of the galaxy as measured from the isophotal fitting show significant variations with radius. According to Bender & Moellenhoff (1987), the interaction between galaxies can cause isophotal twisting, so these variations can be due to the disturbed morphology of the galaxy, added to the fact that the GMOS r'-band image is not deep and star-forming regions and spiral structure are dominating at these wavelengths. If we consider the external isophotes of AM 2322A, the values found are about $\psi_0 = 75^\circ$ and $i = 20^\circ$.

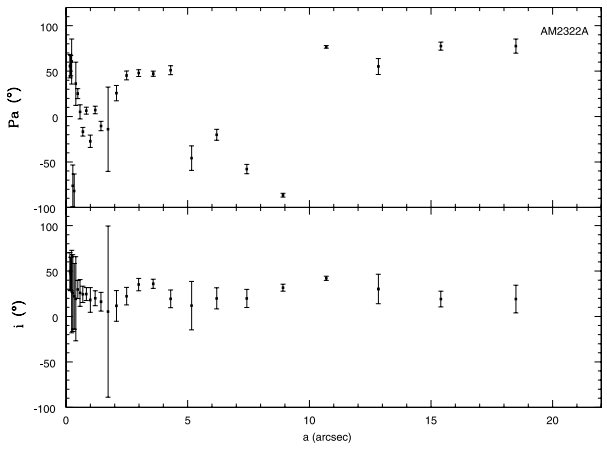

Figure 2. Results of the isophote fitting as a function of the distance along the major axis a in arcseconds for AM 2322A. Top panel: inclination of the galaxy. Bottom panel: position angle of the major axis.

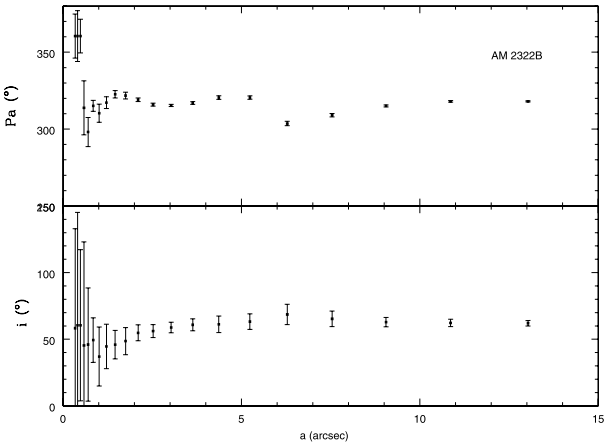

Figure 3. Same as Fig. 2, but for AM 2322B.

Ferreiro & Pastoriza (2004) estimated the inclination of the galaxies in this pair, measuring the major and minor diameters of the 24 mag arcsec^{-2} isophote from images in the B filter. They found $i = 44^\circ$ and 54° for AM 2322A and AM 2322B, respectively.

The rotation curves and the spatial profiles of the Hα emission and λ 5735 continuum flux along the observed slit positions are presented in Figs 4 and 5 for AM 2322A and AM 2322B, respectively.

As can be seen in Fig. 4, AM 2322A does not have a well-defined and symmetric rotation curve along to the observed slit positions, indicating that the inclination of the galaxy must be quite low and that this object is actually being seen near face-on. Then, the real inclination of the galaxy must be lower than the one obtained from Ferreiro & Pastoriza (2004) and perhaps even from our own estimation.

The heliocentric velocity of the main galaxy is taken to be the radial velocity measured at the nominal centre (continuum peak) along the slit position at PA $= 59^\circ$ or $v_r = 3739$ km s^{-1}.

AM 2322B shows a fairly symmetric rotation curve and for this galaxy we adopted a very simple approximation for the observed velocity distribution, assuming that the gas moves under a logarithmic gravitational potential, following circular orbits close to a plane $P(i, \psi_0)$, characterized by its inclination to the plane of the sky (i) and the position angle (PA) of the line of nodes ψ_0. This assumption results in an observed radial circular velocity $v(r, \psi)$ in the plane of the sky given by Bertola et al. (1991):

$$v(r, \psi) = V_\mathrm{s} + \frac{V_0 R \cos(\psi - \psi_0)\sin(i)\cos(i)}{\sqrt{R^2\eta + R_\mathrm{c}^2\cos^2(i)}} \quad (1)$$

with

$$\eta \equiv [\sin^2(\psi - \psi_0) + \cos^2(i)\cos^2(\psi - \psi_0)], \quad (2)$$

where V_s is the systemic velocity, R is the radius in the plane of the galaxy, and V_0 and R_c are parameters that define the amplitude and shape of the curve. The fit of the rotation curve for this galaxy is shown in Fig. 5, and the parameters obtained from the fits are shown in Table 2.

The above model for the rotation curve results in a heliocentric velocity of 3376 km s^{-1}. The observed radial velocities along the major axis are well represented by the model. The rotation curve is

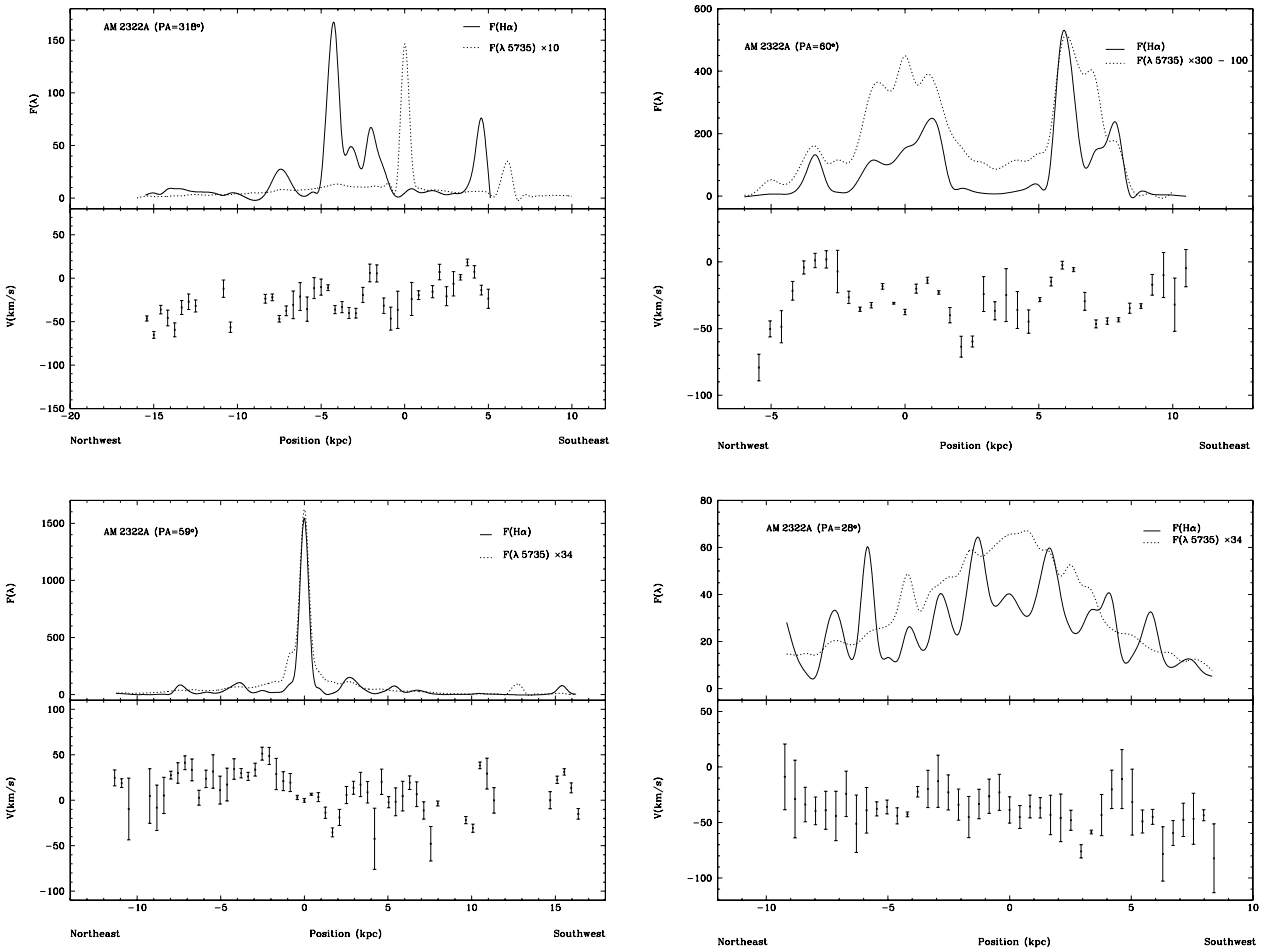

Figure 4. Observed Hα and λ 5735 flux (in units of 10^{-17} erg cm^{-2} s^{-1}) and mean radial velocity as a function of the distance to the centre of the slit along PA = 318°, 60°, 59° and 28° for AM 2322A. The velocity scale corresponds to the observed and model values after subtraction of the systemic velocity of the galaxy, without correction by the inclination in the plane of the sky.

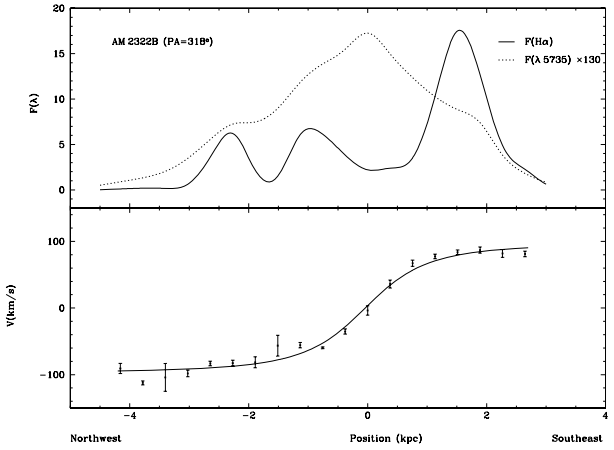

Figure 5. Observed Hα and λ 5735 flux (in units of 10^{-17} erg cm^{-2} s^{-1}) and mean radial velocity as a function of apparent galactocentric distance along PA = 318° for AM 2322B. The velocity scale corresponds to the observed and model values after subtraction of the systemic velocity of the galaxy, without correction by the inclination in the plane of the sky.

typical of spiral discs, rising shallowly and flattening at an observed amplitude of 110 km s^{-1}, with small (less than 25 km s^{-1}) deviations from the smooth rotational field, which are commonly observed in interacting galaxies.

Table 2. Kinematical parameters for AM 2322B.

Parameter	AM 2322B (PA = 318°)
i (°)	63
ψ_0 (°)	318
V_s (km s^{-1})	3 376 ± 6
V_0 (km s^{-1})	110 ± 6
R_c (kpc)	−0.33 ± 1391

Donzelli & Pastoriza (1997) estimated systemic velocities of 3680 and 3424 km s^{-1} for AM 2322A and AM 2322B, respectively, which agree within 2 per cent with our values.

For AM 2322B, we can obtain an estimation of the dynamical mass by assuming that the mass inside a certain radius is given by $M(R) = RV^2/G$. Using the deprojected velocity amplitude of 110 km s^{-1} and a radius of 4 kpc, its dynamical mass is 1.12×10^{10} M$_\odot$. It is important to emphasize that the maximum radius to which we can observe the gas in emission is quite certainly smaller than the total radius of the galaxies, so our estimate of the dynamical mass is a lower limit to the actual dynamical mass of the system. The estimation of the deprojected velocity is also dependent on the assumed inclination of the galaxies with respect to the plane of the sky, so if we assume the inclination angle of $i = 54°$ as derived by

Ferreiro & Pastoriza (2004), the dynamical mass would be $1.36 \times 10^{10}\,M_{\odot}$.

4 NUMERICAL SIMULATIONS

Aiming to reconstruct the history of the AM 2322−821 system and predict its evolution, we attempted to reproduce the interaction between AM 2322A and AM 2322B by running a series of *N*-body simulations. The simulations were carried out with the *N*-body/SPH code GADGET-2 developed by Springel (2005). Galaxies were modelled following the prescription of Hernquist (1993), where we included a gaseous disc component.

The model parameters for AM 2322B were constrained from the observed morphology and rotation curve presented in Section 3. The resulting simulated rotation curve is shown in Fig. 6, where we overplot the observed circular velocity data.

In order to build a model for AM 2322A, we first attempted to measure its inclination through isophotal ellipse fitting (see Fig. 2), but the results are inconclusive due to the small inclination angle, combined with tidal distortions experienced by the galaxy, which result in strong radial variations on the resulting isophotal position angle. The long-slit spectra cross the disc through two different position angles (see Figs 1 and 4), and none of those shows a clear sign of rotation, so the rotation curve cannot really be used to constrain the mass distribution of the galaxy as in the case of AM 2322B. AM 2322A is modelled as a face-on galaxy. A photometric mass estimate of $1.7 \times 10^{11}\,M_{\odot}$ is obtained using an absolute B magnitude $M_B = -20.98$ (Ferreiro & Pastoriza 2004) and assuming a mass-to-light ratio of $\gamma_B = 4.4\,M_{\odot}\,L_{\odot}^{-1}$ from Faber & Gallagher (1979) as valid for a Hubble type SA(r)c galaxy (de Vaucouleurs et al. 1991).

As usual in this kind of approach, to reproduce the dynamical and morphological state of the AM 2322−821 system we have to solve the reverse problem of finding the orbit followed by the galaxies from their observed properties, and this is not a fully determined problem, since the observational data do not provide all the necessary information. Therefore, in order to set up the initial conditions for the simulations, we calculate orbits that satisfy the requirements given by the observed radial velocity difference, testing different eccentricities, pericentre distances and line-of-sight direction distances. After that, based on the observed morphology and previous experience, we select a few orbits to simulate, from which the one that best fits the observed properties is selected.

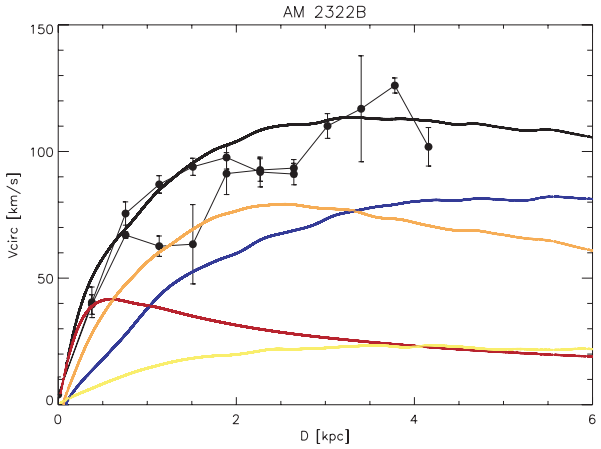

Figure 6. Circular velocity curve of the initial model for AM 2322B (initial condition for the simulation). Rotation curves of the individual components are shown: spherical halo in orange, bulge in red, stellar disc in blue and gas disc in yellow. The total rotation curve is the continuous thick black line. Points with error bars connected by thin black line segments are the observed radial velocity values.

Table 3. Parameters used on the simulations.

	AM 2322A	AM 2322B
Number of points in disc	16384	8192
Disc mass	0.6	0.08
Disc radial scalelength	0.7	0.3
Disc vertical scale thickness	0.14	0.0
Reference radius $R_{\rm ref}$	1.7	0.8
Toomre Q at $R_{\rm ref}$	1.5	1.5
Number of points in gas disc	16384	8192
Gas disc mass	0.06	0.01
Gas disc radial scalelength	1.0	0.45
Gas disc vertical scale thickness	0.07	0.01
Toomre Q at $R_{\rm ref}$	1.2	1.4
Number of points in bulge	1024	1024
Bulge mass	0.5	0.01
Bulge radial scalelength	0.14	0.05
Number of points in spherical halo	16384	8192
Halo mass	2.4	0.24
Halo cut-off radius	6.0	2.0
Halo core radius	0.6	0.4

Note. Simulations were done in a system of units with $G = 1$. Model units scales to physical ones such that length unit is 3.5 kpc, unit velocity is $262\,{\rm km\,s^{-1}}$, unit mass is $5.586 \times 10^{10}\,M_{\odot}$ and unit time is 13.062 Myr.

Different galaxy models were tested, and the parameters of the final ones are presented in Table 3. The AM 2322A model has a total mass of $1.7 \times 10^{11}\,M_{\odot}$, and the mass of the AM 2322B model is $1.6 \times 10^{10}\,M_{\odot}$. The mass of each individual component (disc, bulge, halo and gas) of both models is also given in the table. The disc inclination in the models was chosen to match the observationally derived values (see Section 3: AM 2322A is modelled as a face-on galaxy). The determination of the AM 2322B model inclination required several test simulations, because the tidal distortions and warping induced by the interaction modify the projected axial ratio: the initial conditions with the AM 2322B model inclined by $i = 68^{\circ}$ led to final morphologies that do not match with the observed one. The best results were obtained with AM 2322B initially inclined by $i = 80^{\circ}$. A total of 75 776 particles were used.

After several runs, the orbit that best reproduces the observational properties is a fast hyperbolic orbit, with an eccentricity $e = 3.1$ and perigalacticon of $q = 10.5$ kpc. The orbital plane is inclined to the plane of the sky by 37°, and intersects the latter at a position angle of 80°.

The dynamical mass of AM 2322B, as obtained in Section 2 up to a radius of 4 kpc, amounted to $1.12 \times 10^{10}\,M_{\odot}$. At the final stage of the simulation, up to that radius, the model provided a mass of $1.1 \times 10^{10}\,M_{\odot}$ (the initial model has a mass of $1.22 \times 10^{10}\,M_{\odot}$ up to that radius).

The simulation indicates that the spatial distance between the two galaxies is 43.8 kpc (sky projected distance is 35 kpc). AM 2322A is closer to us than AM 2322B.

Radial velocity curves of model galaxies AM 2322A and AM 2322B are presented in Fig. 7. They are compared with the observed radial velocity data and show that the kinematics of the models is correct.

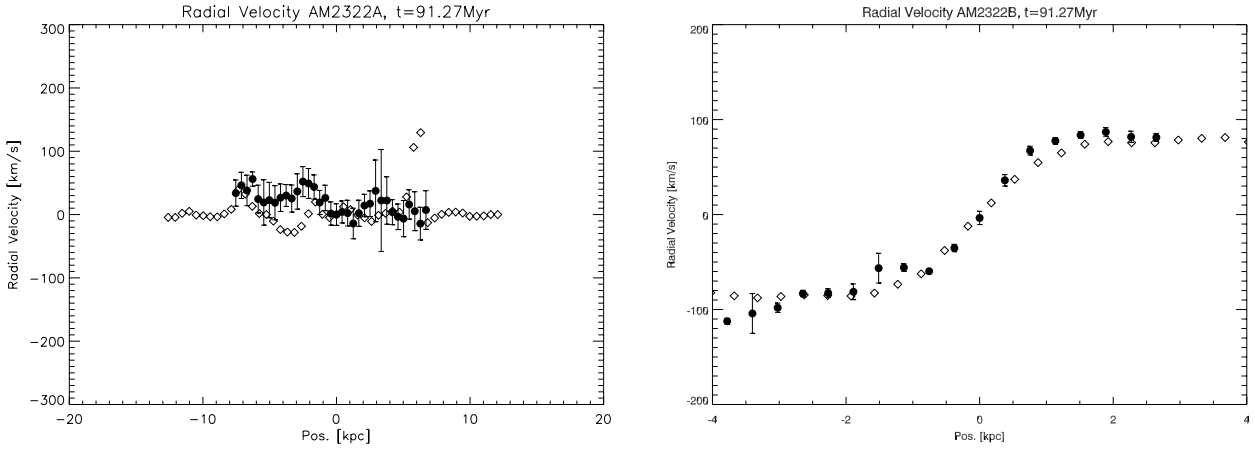

Figure 7. Radial velocity curves of the models at the final stage, taken at the same position angles as the observed ones, for comparison. Left-hand and right-hand panels are for AM 2322A and AM 2322B, respectively. Lozenges are from the simulations, black dots with error bars are from observations.

Fig. 8 shows the time evolution of the encounter. Time is shown in Myr in the upper-right corner of each frame, with respect to the perigalacticon. The simulation starts ∼120 Myr before perigalacticon. The situation that best reproduces the morphology and kinematics of the present stage of the AM 2322−821 system is at $t = 91.27$ Myr after perigalacticon. The general large-scale morphology and kinematics agree well with observations, within the resolution provided by the simulations.

5 STELLAR POPULATION SYNTHESIS

A detailed study of the star formation in minor merger galaxies is an important source of information not only on the age distribution of their stellar population components, but also to better understand several aspects of the interaction process, its effect on the properties of the individual galaxies and their later evolution. The absorption features arising from the stellar component also affect to different degrees the measured intensity of the emission line in the spectrum of the gaseous component. This effect is more prominent in, but not restricted to, the Balmer lines, so the stellar population contribution must be subtracted from each spectrum in order to study the physical properties of the gas.

To investigate the star formation history of AM 2322A and AM 2322B, we use the stellar population synthesis code STARLIGHT (Cid Fernandes et al. 2004, 2005; Mateus et al. 2006; Asari et al. 2007). This code is extensively discussed in Cid Fernandes et al. (2004, 2005), and is built upon computational techniques originally developed for empirical population synthesis with additional ingredients from evolutionary synthesis models. The code fits an observed spectrum O_λ with a combination of $N_\star$ single stellar populations (SSPs) from the Bruzual & Charlot (2003) models. These models are based on a high-resolution library of observed stellar spectra, which allows for detailed spectral evolution of the SSPs at a resolution of 3 Å across the wavelength range of 3200–9500 Å with a wide range of metallicities. We used the Padova 1994 tracks as recommended by Bruzual & Charlot (2003), with the initial mass function of Chabrier (Chabrier 2003) between 0.1 and 100 $M_\odot$. Extinction is modelled by STARLIGHT as due to foreground dust, using the reddening law of Cardelli, Clayton & Mathis (1989) with $R_V = 3.1$, and parametrized by the V-band extinction A_V. The SSPs used in this work cover 15 ages, $t = 0.001$, 0.003, 0.005, 0.01, 0.025, 0.04, 0.1, 0.3, 0.6, 0.9, 1.4, 2.5, 5, 11 and 13 Gyr, and three metallicities, $Z = 0.2$, 1 and 2.5 $Z_\odot$, summing up to 45 SSP components.

Briefly, the code solves the following equation for a model spectrum $M_\odot$ (Cid Fernandes et al. 2005):

$$M_\lambda = M_{\lambda 0}\left[\sum_{j=1}^{N_\star} x_j b_{j,\lambda} r_\lambda\right] \otimes G(v_\star, \sigma_\star), \quad (3)$$

where $b_{j,\lambda}$ is the reddened spectrum of the jth SSP normalized at λ_0; $r_\lambda = 10^{0.4(A_\lambda - A_{\lambda_0})}$ is the reddening term; $M_{\lambda 0}$ is the synthetic flux at the normalization wavelength; $\boldsymbol{x}$ is the population vector; $\otimes$ denotes the convolution operator; and $G(v_\star, \sigma_\star)$ is the Gaussian distribution used to model the line-of-sight stellar motions – it is centred at velocity $v_\star$ with dispersion $\sigma_\star$.

The fit is carried out with a simulated annealing plus Metropolis scheme, which searches for the minimum of the equation (Cid Fernandes et al. 2005)

$$\chi^2 = \sum_\lambda [(O_\lambda - M_\lambda) w_\lambda]^2, \quad (4)$$

where emission lines and spurious features are masked out by fixing $w_\lambda = 0$. For more details on STARLIGHT, see Cid Fernandes et al. (2005).

Prior to the modelling, the SSP models were convolved to the same resolution as the observed spectra; the observed spectra were shifted to their rest frame, corrected for foreground Galactic reddening of $E(B - V) = 0.181$ mag taken from Schlegel, Finkbeiner & Davis (1998) and normalized to λ 5870 Å. The error in O_λ considered in the fitting was the continuum rms with an S/N ≥ 10, where S/N is the signal-to-noise ratio per Å in the region around $\lambda_0 =$ 5870 Å. Also, the fitting was performed only in spectra with the presence of absorption lines. Measurement errors are still a problem in population synthesis. The most serious drawback of STARLIGHT, as it is, is that it does not provide error estimates on its parameters. The reliability of parameter estimation was best studied in Cid Fernandes et al. (2004, 2005) by means of simulations which fed the code with spectra generated with known parameters, added noise and then examined the correspondence between the input and output values. They performed this kind of simulation for an $N_\star = 20$ base and the main results of that study were: (1) in the absence of noise, the method recovers all components of $\boldsymbol{x}$ to a high degree of accuracy; (2) in the presence of noise, however, the individual output x_j fractions may deviate drastically from the input values. However, this problem can be circumvented by binning the stellar populations according to the flux contributions. In addition, the absorption features present in our spectra, i.e. Balmer lines, are mainly dependent

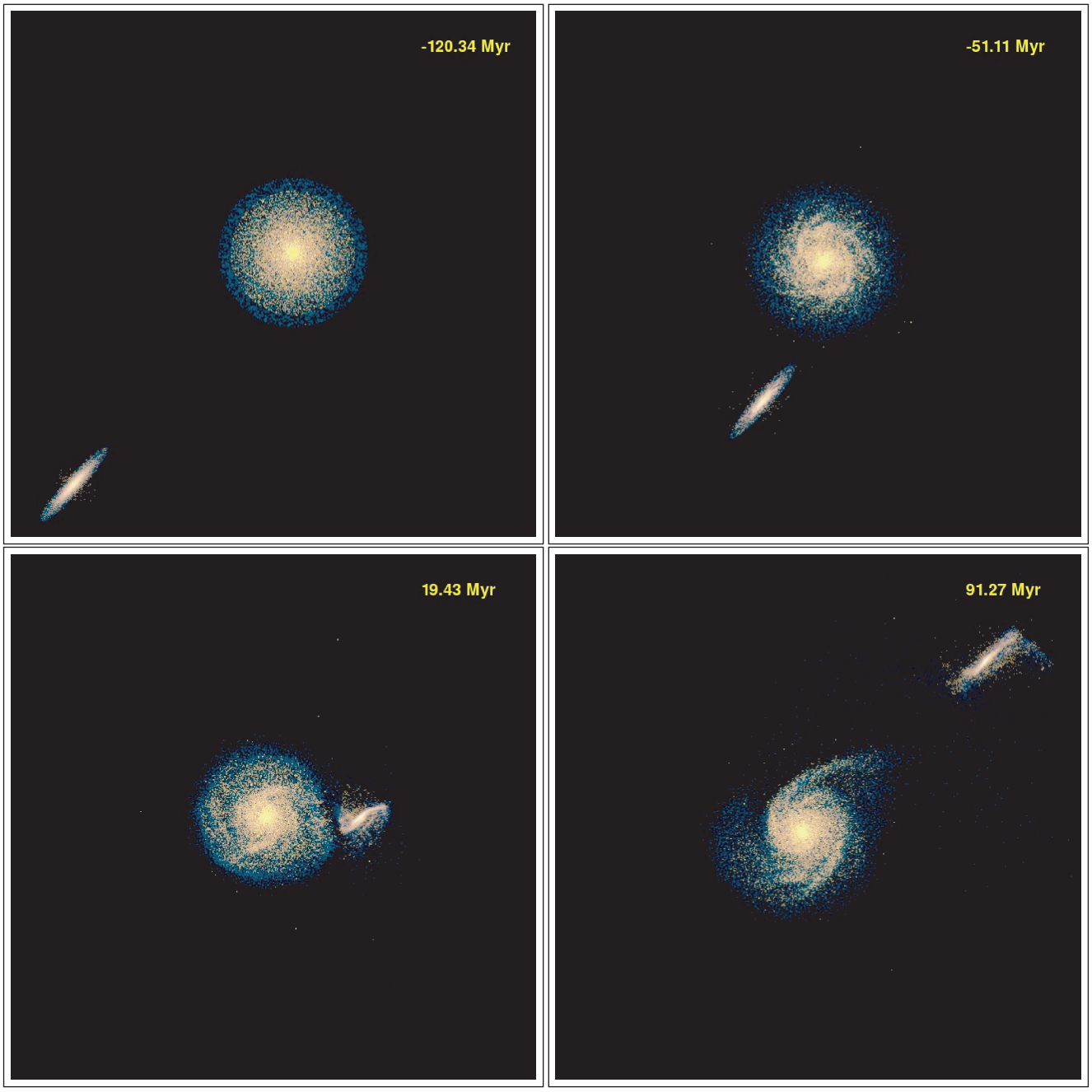

Figure 8. Time evolution of the encounter. Time is shown in Myr in the upper-right corner of each frame, with respect to the orbital pericentre. The simulation begins at the upper-left frame. Stars are shown in light colours, while the gas is shown in blue. The dark matter halo is not shown. The best fit to the current state of the AM 2322−821 system is shown in the last frame.

on age rather than on metallicity. Fig. 9 is a histogram of the contribution of each stellar population to the optical flux λ 5870 Å of the spectrum of the central region along PA = 59°, before binning the stellar populations. About the same results were obtained for the other apertures. It can be noted in Fig. 9 that about the same contributions by age are obtained from different metallicities, with a little increase in the old population contribution when lower Z values are assumed (the metallicity–age degeneracy problem).

Fig. 10 shows an example of the observed spectra corrected for reddening, the model stellar population spectra and the pure emission spectra for AM 2322A and AM 2322B. The results of the synthesis are summarized in Tables 4 and 5 for the individual spatial bins in each galaxy, stated as the percentage contribution of each base element to the flux at λ 5870 Å.

Following the prescription of Cid Fernandes et al. (2005), we defined a condensed population vector, by binning the stellar populations according to the flux contributions into very young, $x_{\rm VY}$ ($t \leq 1 \times 10^8$ yr); young, $x_{\rm Y}$ ($1 \times 10^8 < t \leq 5 \times 10^8$ yr); intermediate-age, $x_{\rm I}$ ($5 \times 10^8 < t \leq 2 \times 10^9$ yr); and old, $x_{\rm O}$ ($t > 2 \times 10^9$ yr) components. The same bins were used to represent the mass components of the population vector ($m_{\rm VY}$, $m_{\rm Y}$, $m_{\rm I}$ and $m_{\rm O}$). The metallicity, an important parameter to characterize the stellar population content, is weighted by light fraction, and the results point to a mean value around solar. The quality of the fitting

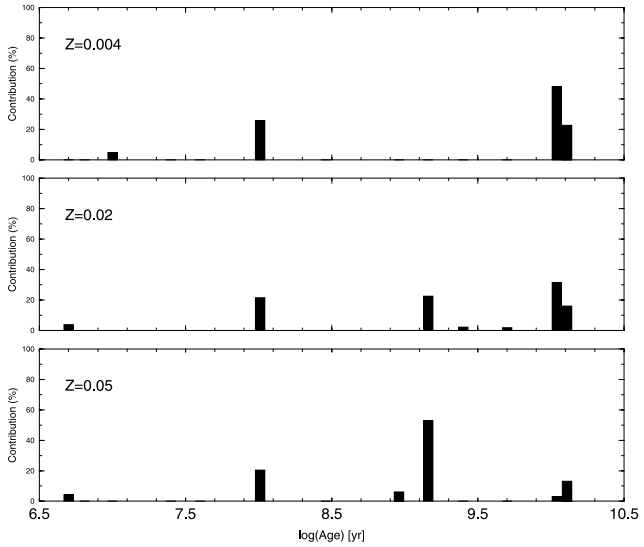

Figure 9. Histogram for the central region along PA = 59° showing the contribution to the flux continuum (as percentage of each stellar age component for the three metallicity values considered).

result is measured by the parameters χ^2 and *adev*. The latter gives the percentage mean deviation $|O_\lambda - M_\lambda|/O_\lambda$ over all the fitted pixels, where O_λ and M_λ are the observed and model spectra, respectively.

The spatial variation in the contribution of the stellar population components is shown in Figs 11 and 12 for the galaxies AM 2322A and AM 2322B, respectively.

As can be seen in Fig. 11, the stellar population of AM 2322A is heterogeneous along both the slit positions. It does not show an age gradient: the very young $x_{\rm VY}$, intermediate $x_{\rm I}$ and old populations $x_{\rm O}$ contribute significantly to the optical flux at λ 5870 Å. In a mass-weighted context, the bulge is predominantly composed of old population, in agreement with the results obtained by MacArthur, González & Courteau (2009).

AM 2322B is dominated by the very young population component $x_{\rm VY}$. This component has a systematic variation along the slit, increasing outwards. The fraction of old and intermediate stellar population components is found to be decreasing from the centre to the outer region. The young star formation episode that occurred in this galaxy could be related to the perigalactic passage, that is, about 90 Myr after perigalacticon. The effects of the galaxy interaction in the star formation history are much more conspicuous in the secondary galaxy than in the main galaxy. This is expected as the triggering of star formation events by tidal interactions appears to be more efficient in less massive systems. Similar results were also found for the pair AM 2306−721 (Krabbe et al. 2008).

6 GAS PHASE O/H ABUNDANCE

Once the stellar population contribution has been determined, the underlying absorption line spectrum can be subtracted to allow the measurement and analysis of the line emission from the gaseous component. The line intensities were measured using Gaussian line profile fitting on the pure emission spectra. We used the IRAF SPLOT routine to fit the lines, with the associated error given as $\sigma^2 = \sigma^2_{\rm cont} + \sigma^2_{\rm line}$, where $\sigma_{\rm cont}$ and $\sigma_{\rm line}$ are the continuum rms and the Poisson error of the line flux, respectively. The relative error in the flux estimates of the emission lines is lower than 20 per cent. The residual extinction associated with the gaseous component for each spatial bin was calculated comparing the observed Hγ/Hβ and Hα/Hβ ratios with the theoretical values in Hummer & Storey (1987) for an electron temperature of 10 000 K and an electron density of 100 cm^{-3}. The observed emission line intensities were then corrected by this residual extinction using the Howarth (1983) reddening function.

Determining accurate element abundances of the gas phase from optical spectra is critically dependent on obtaining temperature-sensitive line ratios, such as [O III](λ 4959 + λ 5007)/λ 4363. However, when doing spectroscopy of H II regions with high metallicity and/or low excitation, temperature-sensitive lines such as [O III]λ 4363 are found to be weak or unobservable, and empirical indicators based on more easily measured line ratios have to be used to estimate metal abundances.

Because we did not detect any temperature-sensitive emission lines in our spectra, we used the R_{23} = ([O II]λ 3727+[O III] λ 4959+[O III] λ 5007)/Hβ versus [O III]λ 5007/[O II]λ 3727 (McGaugh 1991) diagnostic diagram to estimate the metallicity of the gas in the star-forming regions by comparing the observed values with a grid of photoionization models. The [N II]λ 6584/[O II]λ 3727 line ratio was used to break the R_{23} degeneracy for our data, as suggested by Kewley & Ellison (2008). We verify that all the observed star-forming regions of our galaxies

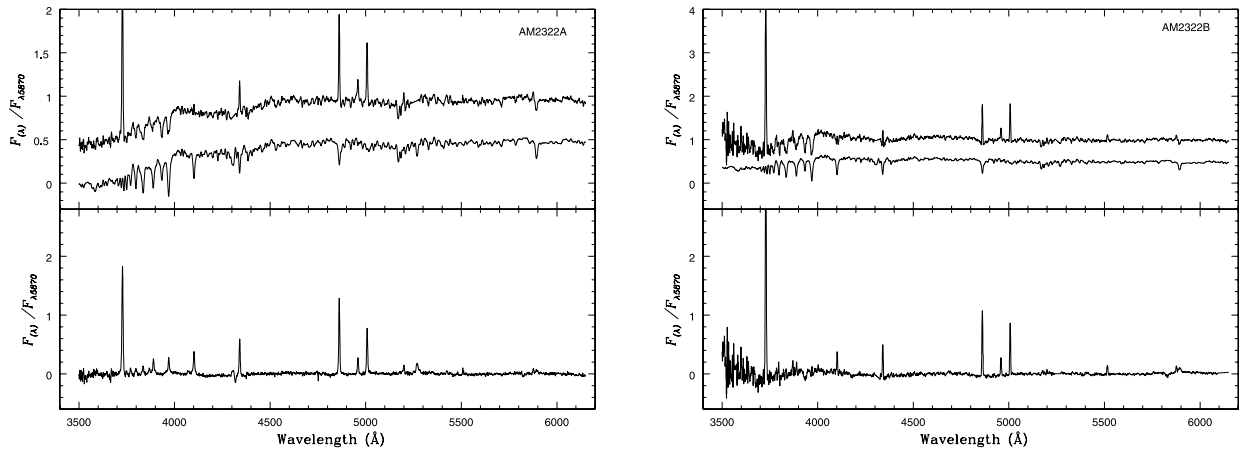

Figure 10. Stellar population synthesis for the central bin along the PA = 59° and 318° slit positions, for AM 2322A (left) and AM 2322B (right), respectively. Top panel: spectrum corrected for reddening and the synthesized spectrum (shifted by a constant). Bottom panel: pure emission spectrum.

Table 4. Stellar population synthesis results for AM 2322A.

Pos. (kpc)	x_{VY} (per cent)	x_Y (per cent)	x_I (per cent)	x_O (per cent)	m_{VY} (per cent)	m_Y (per cent)	m_I (per cent)	m_O (per cent)	$Z_\star$[1]	χ^2	*adev*	A_V (mag)
					AM 2322A (PA = 59°)							
−7.98	14.3	22.8	18.2	40.6	0.4	2.3	3.1	94.2	0.014	1.4	5.83	0.15
−7.56	21.1	26.3	0.0	49.9	0.5	1.8	0.0	97.7	0.028	0.1	7.98	0.00
−7.14	19.9	13.7	10.2	56.6	0.8	1.8	5.7	91.6	0.010	0.1	24.79	0.00
−6.72	9.7	25.9	40.2	21.2	0.2	4.0	12.4	83.4	0.024	0.1	10.96	0.00
−5.88	14.8	0.0	61.8	20.7	0.3	0.0	37.0	62.7	0.007	0.1	13.14	0.42
−5.46	13.2	25.6	29.6	29.4	0.1	3.8	10.2	85.9	0.019	0.0	10.20	0.48
−5.04	8.8	33.4	18.1	37.4	0.1	3.3	3.5	93.1	0.016	0.1	7.65	0.24
−4.62	10.9	38.9	0.0	46.8	0.1	2.2	0.0	97.7	0.021	0.1	5.59	0.25
−4.20	32.3	33.7	14.2	16.8	1.7	10.7	9.4	78.2	0.022	0.1	4.88	0.34
−3.78	19.7	25.5	22.4	31.0	0.4	2.0	5.8	91.8	0.033	0.1	4.95	0.12
−3.36	13.4	6.9	39.1	39.5	0.1	0.7	7.9	91.2	0.022	0.1	5.54	0.18
−2.52	8.8	8.5	43.7	37.6	0.1	0.9	10.3	88.8	0.021	1.2	3.88	0.38
−2.10	0.7	0.0	64.6	33.7	0.0	0.0	11.9	88.1	0.021	0.1	12.37	0.05
−1.68	0.0	17.8	29.5	51.8	0.0	0.8	4.6	94.5	0.017	0.2	22.41	0.21
−1.26	0.0	28.4	26.5	43.7	0.0	1.5	5.1	93.4	0.031	0.1	19.28	0.51
−0.84	1.9	25.8	1.0	69.7	0.0	1.3	0.2	98.5	0.025	0.0	15.76	0.78
−0.42	22.6	28.8	30.8	17.2	2.1	5.4	21.0	71.6	0.018	0.1	7.19	1.40
0	7.1	21.3	10.7	60.7	0.1	1.1	2.9	95.9	0.023	0.0	2.77	0.46
0.42	12.5	15.5	21.9	50.6	0.1	0.8	7.8	91.3	0.024	0.0	3.25	0.39
0.84	6.5	17.9	24.0	51.4	0.0	0.9	7.3	91.7	0.028	0.1	8.98	0.53
1.26	2.3	9.4	35.7	50.8	0.1	0.7	9.2	90.1	0.029	0.1	16.82	0.46
2.10	6.2	27.0	16.0	48.1	0.1	2.4	2.7	94.8	0.021	0.2	31.91	0.24
2.52	9.7	36.7	18.8	33.9	0.1	2.3	3.3	94.3	0.020	0.2	12.53	0.29
2.94	28.4	45.1	0.0	24.4	0.5	3.6	0.0	95.9	0.015	0.2	7.64	0.35
3.36	35.8	23.5	0.0	37.2	0.3	1.6	0.0	98.1	0.032	0.2	7.87	0.23
3.78	28.7	25.0	7.8	37.3	0.6	4.3	2.2	92.9	0.029	0.2	19.06	0.22
					AM 2322A (PA = 28°)							
−4.20	25.2	8.9	0.0	69.0	0.9	1.2	0.0	97.8	0.012	0.1	16.85	0.17
−3.78	25.3	0.0	0.0	73.8	0.4	0.0	0.0	99.6	0.004	0.1	21.13	0.00
−3.36	21.0	16.1	6.6	56.0	0.1	1.5	1.1	97.2	0.013	0.1	11.01	0.09
−2.94	16.6	6.6	29.9	51.6	0.1	0.6	11.5	87.8	0.012	0.1	9.93	0.10
−2.52	11.4	24.6	6.1	64.1	0.3	2.7	3.3	93.7	0.010	0.1	9.77	0.28
−2.1	21.2	56.2	0.0	26.1	0.4	7.4	0.0	92.2	0.026	0.1	9.64	0.53
−1.68	29.0	0.0	73.0	0.0	2.5	0.0	97.3	0.2	0.022	0.1	7.99	0.41
−1.26	10.1	0.0	23.5	68.8	0.2	0.0	8.2	91.5	0.009	0.1	11.85	0.19
−0.84	16.2	0.0	34.5	52.9	0.5	0.0	8.6	90.9	0.007	0.1	8.10	0.37
−0.42	26.6	12.8	3.5	58.4	0.4	1.4	0.9	97.3	0.020	0.1	7.93	0.12
0	14.4	0.0	41.9	42.2	0.6	0.0	14.3	85.1	0.012	0.1	8.07	0.42
0.42	26.9	8.2	14.4	50.0	0.3	0.8	4.3	94.6	0.018	0.1	7.50	0.45
0.84	12.5	47.9	0.0	41.8	0.4	3.6	0.0	96.0	0.026	0.1	6.90	0.54
1.26	30.2	23.6	10.1	36.3	0.5	4.2	5.8	89.5	0.015	0.1	7.32	0.68
1.68	21.3	3.3	49.0	26.0	0.3	0.6	37.0	62.2	0.016	0.1	9.91	0.56
2.10	5.8	44.3	0.9	52.2	0.2	5.4	0.3	94.1	0.007	0.1	39.77	0.76
2.52	19.6	9.7	56.6	8.6	0.8	2.2	46.1	51.0	0.016	0.1	18.30	0.80
3.36	18.4	31.9	0.0	59.3	0.5	5.9	0.0	93.6	0.019	0.1	22.39	0.00
3.78	16.8	0.0	45.6	41.0	0.7	0.0	21.4	77.9	0.022	0.1	30.54	0.23
4.62	22.2	0.6	80.7	0.1	1.6	0.2	97.9	0.2	0.038	0.1	54.97	0.66

[1] Abundance by mass with $Z_\odot = 0.02$.

have log([N II]λ 6584/[O II]λ 3727) > −1, thus they are placed in the upper R_{23} branch.

The photoionization models were built using the code CLOUDY/08.00 (Ferland 2002). In each model, a stellar cluster was assumed as the ionizing source with the stellar energy distribution obtained from the synthesis models STARBURST99 (Leitherer et al. 1999). We calculated models with metallicities of $Z = 2.0$, 1.0, 0.6, 0.4 and 0.2 $Z_\odot$, ionization parameter log $U = -1.0$, −1.5, −2, −2.5, −3.0 and −3.5, with the stellar cluster having an upper stellar mass limit of $M_{up} = 100\ M_\odot$, an age of 2.5 Myr and having been formed by an instantaneous burst. The solar value of $12 + \log(O/H) = 8.69$ is taken from Allende Prieto, Lambert & Asplund (2001). Similar models have been used to describe observational data of H II regions in interacting (Krabbe, Rembold & Pastoriza 2007; Krabbe et al. 2008) as well as in isolated galaxies (Dors & Copetti 2005). The reader is referred to Dors & Copetti (2006) for a full description of the models. Fig. 13 shows the R_{23} versus [O III]λ 5007/[O II]λ 3727 diagram, with the observed values

Table 5. Stellar population synthesis results for AM 2322B.

Pos. (kpc)	x_{VY} (per cent)	x_Y (per cent)	x_I (per cent)	x_O (per cent)	m_{VY} (per cent)	m_Y (per cent)	m_I (per cent)	m_O (per cent)	$Z_\star$[1]	χ^2	*adev*	A_V (mag)
					AM 2322B (PA = 318°)							
−3.36	79.7	7.1	1.8	7.1	5.5	2.3	1.3	91.0	0.021	1.30	3.94	0.37
−2.94	86.1	11.8	0.2	0.0	47.3	49.4	3.2	0.0	0.020	0.01	4.01	0.00
−2.52	54.4	39.4	0.0	5.6	4.0	13.9	0.0	82.1	0.022	0.01	3.49	0.16
−2.10	51.9	21.2	14.1	10.6	2.3	5.3	7.7	84.6	0.026	0.01	3.49	0.10
−1.88	46.3	9.9	27.5	14.2	2.6	2.9	15.6	78.9	0.022	0.01	3.26	0.00
−1.26	35.4	5.7	29.9	28.3	0.5	0.9	7.1	91.6	0.018	0.01	2.77	0.00
−0.84	28.8	0.8	35.4	33.7	0.4	0.1	8.2	91.3	0.019	0.01	2.71	0.12
−0.42	30.7	0.1	27.3	42.0	0.4	0.0	5.0	94.6	0.022	0.01	2.74	0.28
0	34.2	0.0	32.9	32.9	0.5	0.0	6.9	92.7	0.021	0.01	2.67	0.54
0.42	44.7	0.0	30.6	24.2	0.9	0.0	7.8	91.3	0.022	0.01	2.67	0.53
0.84	63.8	8.8	0.0	26.0	1.7	2.2	0.0	96.2	0.025	0.01	2.83	0.46
1.26	65.8	0.0	19.5	13.5	2.3	0.0	7.1	90.6	0.021	0.01	3.02	0.32
1.68	59.9	27.6	0.0	10.9	5.3	11.2	0.0	83.5	0.018	0.01	2.96	0.32
2.10	37.1	50.7	0.1	11.9	3.2	21.6	0.3	75.0	0.018	0.01	3.89	0.53

[1] Abundance by mass with $Z_\odot = 0.02$.

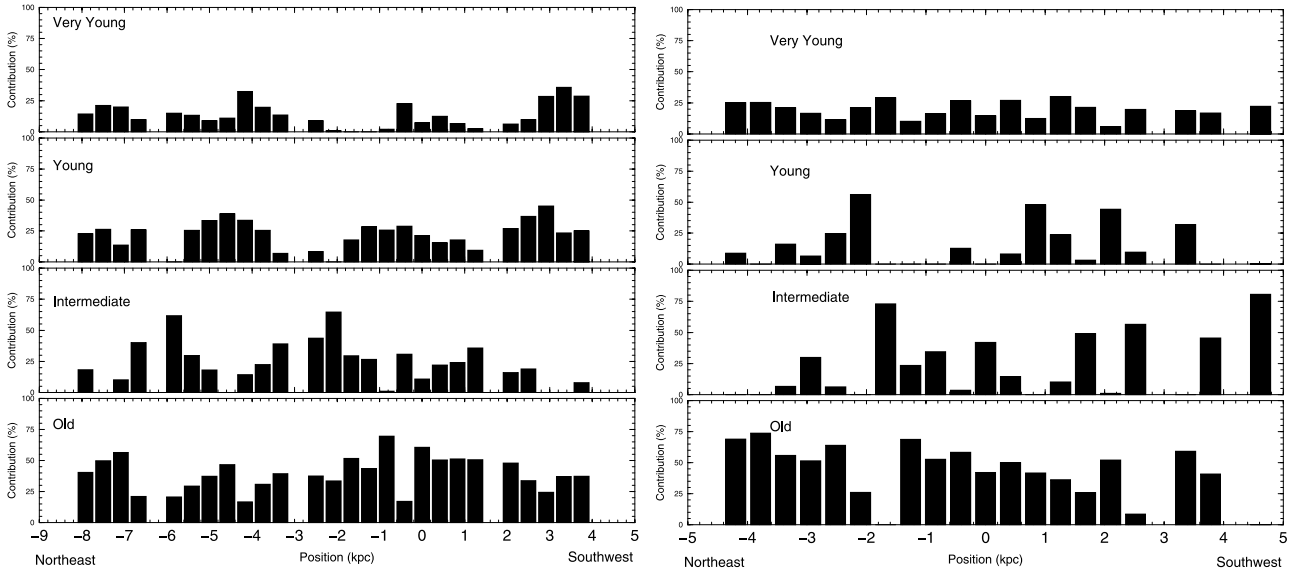

Figure 11. Synthesis results in flux fractions as a function of the distance to the centre of the slit along PA = 59° (left) and PA = 28° (right) for AM 2322A.

superposed in the grid of computed models. Filled squares correspond to regions in AM 2322A and open squares to regions in AM 2322B.Figs 14 and 15 show the estimated O/H abundance distribution as a function of the galactocentric distance for AM 2322A and AM 2322B, respectively.

As we can see in Figs 14 and 15, the oxygen abundances derived from the R_{23} versus [O III]/[O II] diagram suggest a relatively homogeneous O/H value of 8.6(±0.01) and 8.40(±0.05) across the disc of the galaxies AM 2322A and AM 2322B, respectively.

The central O/H values of the two galaxies are lower than those obtained for field galaxies of the same luminosity, in agreement with the results obtained by Kewley et al. (2006) for galaxy pair members with small projected separations ($s < 20$ kpc). This result provides strong observational evidence for the hypothesis that the galaxy interactions create gas flows towards the central regions, carrying less enriched gas from the outskirts of the galaxy into the central regions, mixing and homogenizing the chemical composition of the interstellar medium (Kewley et al. 2006). This is also similar to the result previously found for the AM 2306−721 pair (Krabbe et al. 2008), where the companion galaxy also presented an oxygen abundance relatively homogeneous across the disc.

We compare the metallicity gradients obtained for AM2322A and AM2322B with the gradients for the sample of close pairs derived by Kewley et al. (2010) and for the isolated galaxies M101, Milky Way, M83 and NGC 300. The galactocentric distance is given in units of R/R_{25}, where R_{25} is the B-band isophote at a surface brightness of 25 mag arcsec^{-2}. The R_{25} adopted for AM2322A and AM2322B are 13.5 and 4.2 kpc, respectively. Kewley et al. (2010) computed the gradients using the [N II]λ6584/[O II]λ3727–O/H relation for the first three isolated galaxies and for their sample pair. The metallicity gradient in NGC 300 was computed using the emission line intensities of H II regions obtained by Bresolin et al. (2009) and also using the method cited above. These gradients are shown in Fig. 16. For consistency, we recalculate the gradients in AM2322A and AM2322B using the same method and find $(\frac{12+\log(O/H)}{R/R_{25}}) = -0.13(\pm0.03)$ and $(\frac{12+\log(O/H)}{R/R_{25}}) = -0.36(\pm0.03)$, respectively. As can be seen in Fig. 16, these gradients have about the same slope as close pairs (~-0.25) and are flatter than the

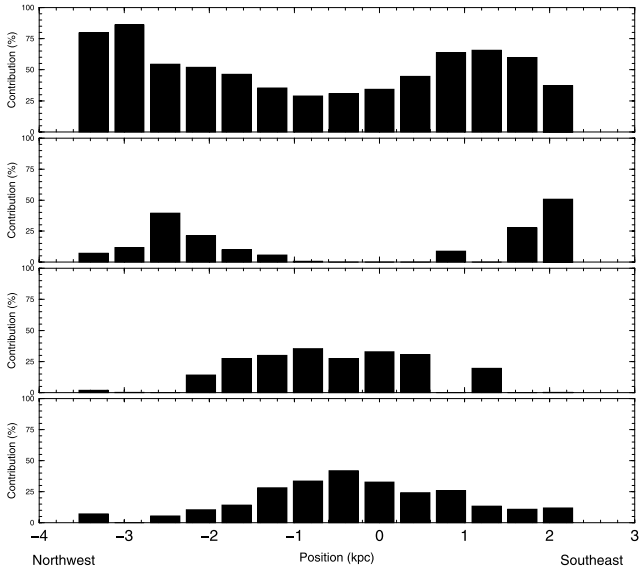

Figure 12. Same as Fig. 10, but along PA = 318° of AM 2322B.

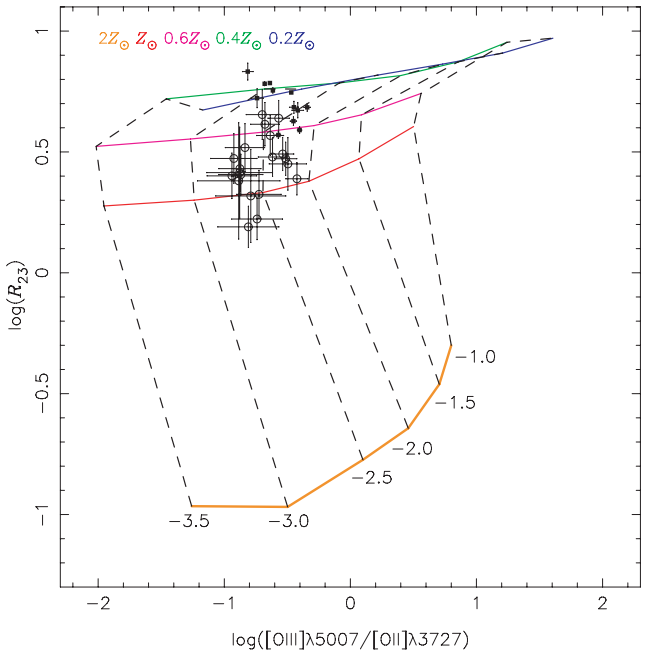

Figure 13. The relation $\log(R_{23})$ versus $\log([\mathrm{O\,III}]/[\mathrm{O\,II}])$ for the individual spatial bins in AM 2322B (filled squares) and AM 2322A (open triangles). The curves represent the photoionization models described in the text (dashed lines correspond to different values of the logarithm ionization parameter, solid lines to different gas metallicities).

gradients in the isolated galaxies (∼−0.57). These results are in agreement with those found by Kewley et al. (2010) in galaxy pairs. We interpreted that these shallower gradients can be explained by the action of inward and outward radial flows of interstellar gas (Krabbe et al. 2008). In isolated spirals, this mechanism seems to be weak or non-existent.

N-body/SPH numerical simulations of equal-mass mergers predict that the radial metallicity gradients of the disc galaxies should flatten shortly after the first pericentre, due to radial mixing of gas (Rupke et al. 2010). Although AM 2322−821 is a system composed of galaxies of quite different mass ($M_{\mathrm{primary}}/M_{\mathrm{secondary}} \approx 11$ from

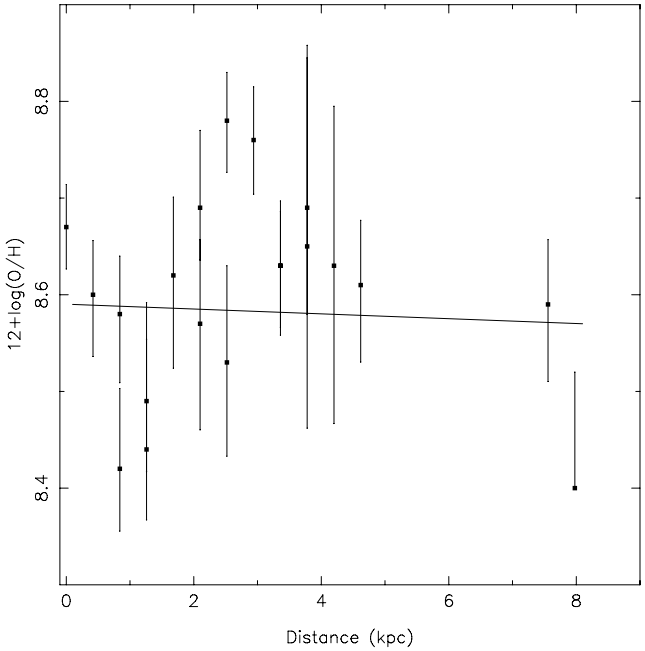

Figure 14. The O/H abundance distribution as a function of the distance to the centre of the AM 2322A estimated using $\log(R_{23})$ versus $\log([\mathrm{O\,III}]/[\mathrm{O\,II}])$. The solid line represents the linear fit of the data.

the models in Section 4), our numerical simulations indicate that the current stage of the merger is about 90 Myr after the first passage, which agrees with the scenario proposed by the above authors.

In our previous work (Krabbe et al. 2008), we found that for the AM 2306−721 pair only the companion galaxy presented an oxygen abundance relatively homogeneous across the disc, while the main galaxy showed a clear radial oxygen abundance gradient. Both the systems, AM 2306−721 and AM 2322−821, are morphologically similar. Each system is composed of a spiral and an irregular galaxy. However, the mass ratio estimated from the numerical simulations for AM 2306−721 is $M_{\mathrm{primary}}/M_{\mathrm{secondary}} \approx 2$ and for AM 2322−821 is about 11; and the numerical simulations predicted that the evolution of the encounter was more violent and slower in AM 2306−721. Then if we assumed that there was an oxygen abundance gradient before the encounter in the main galaxies in both the systems, why was the gradient not destroyed or flattened by the gas inflow in the main galaxy in AM 2306−721? One important point is that the star formation rate in the nuclear region of the main galaxy of AM 2306−721 is about 10 times higher than the one derived for AM 2322−821. These high star formation rates could have increased the heavy element content in the central regions and thus could have produced steeper gradients, and in these cases, a high gas inflow rate would be necessary to destroy or flatten the abundance gradient in the main galaxy of AM 2306−721.

7 CONCLUSIONS

An observational study of the effects of the interaction on the kinematics, stellar population and abundances of the galaxy pair AM 2322−821 was conducted. The data consist of long-slit spectra in the wavelength range of 3350–7130 Å obtained with the Gemini Multi-Object Spectrograph at Gemini South. The main findings are the following.

(i) A fairly symmetric rotation curve for the companion (AM 2322B) galaxy with a deprojected velocity amplitude of

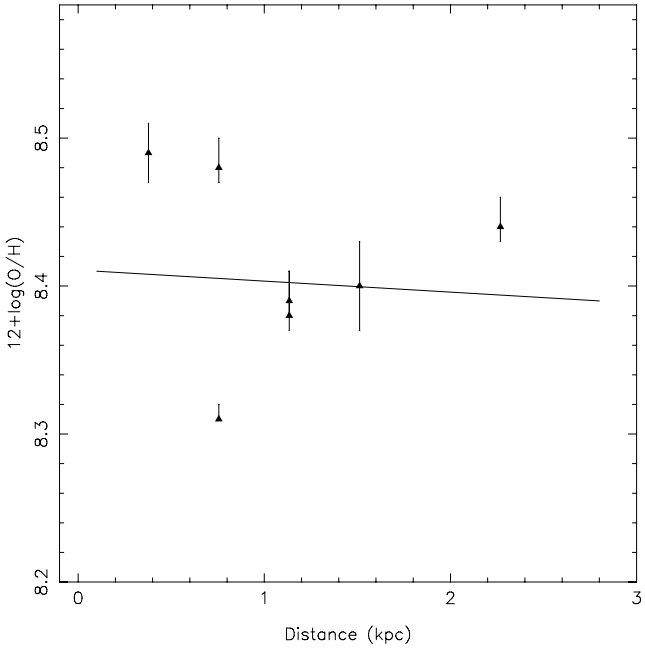

Figure 15. Same as Fig. 14, but for AM 2322B.

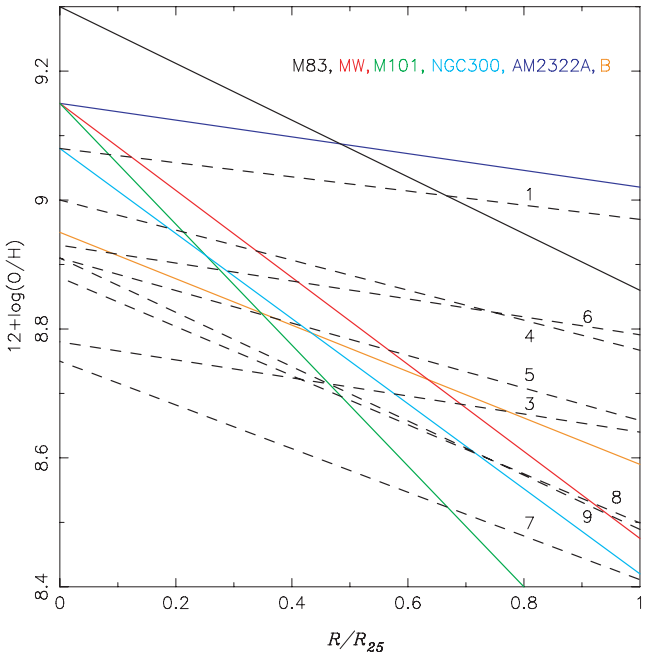

Figure 16. Metallicity gradients for AM2322A (blue line) and AM2322B (orange line). For comparison, we show the metallicity gradients for the isolated galaxies M101 (green line), Milky Way (red line), M83 (filled black line), NGC 300 (cyan line) and eight interacting galaxies (dashed black lines).

110 km s^{-1} is obtained, and a dynamical mass of 1.1–1.3 $\times$ 10^{10} M$_\odot$ within a radius of 4 kpc can be estimated using this deprojected velocity.

(ii) Asymmetries in the radial velocity field were detected for the companion, very likely due to the interaction between the galaxies.

(iii) In order to reconstruct the history of the AM 2322−821 system and to predict the evolution of the encounter, we modelled the interaction between AM 2322A and AM 2322B through numerical *N*-body/hydrodynamical simulations. The orbit that best reproduces the observational properties is found to be hyperbolic, with an eccentricity $e = 3.1$ and perigalacticon of $q = 10.5$ kpc; the current stage of the system would be about 90 Myr after perigalacticon.

(iv) The companion galaxy is dominated by a very young ($t \leq 1 \times 10^8$ yr) population, with the fraction of this population to the total flux at λ 5870 Å increasing outwards in the galaxy disc.

(v) The stellar population of AM 2322A is heterogeneous along the slit positions observed.

(vi) The oxygen abundance spatial profiles obtained for both galaxies are relatively homogeneous across the galaxy discs. The absence of an abundance gradient in these galaxies is interpreted as its having been destroyed by interaction-induced gas flows from the outer parts to the centre of the galaxy.

ACKNOWLEDGMENTS

This study is based on observations made at the Gemini Observatory, which is operated by the Association of Universities for Research in Astronomy, Inc., under a cooperative agreement with the NSF on behalf of the Gemini partnership: the National Science Foundation (United States), the Science and Technology Facilities Council (United Kingdom), the National Research Council (Canada), CONICYT (Chile), the Australian Research Council (Australia), Ministério da Ciencia e Tecnologia (Brazil) and SECYT (Argentina).

The authors would like to thank Volker Springel for providing them with GADGET-2. IR also acknowledges Instituto Nacional de Pesquisas Espaciais – INPE/MCT, Brazil, for providing computer time in one of its clusters to run the simulations presented here. ACK acknowledges the support of FAPESP, process 2010/01490-3.q

We also thank Ms Alene Alder-Rangel for editing the English in this manuscript.

REFERENCES

Allende Prieto C., Lambert D. L., Asplund M., 2001, ApJ, 556, L63
Asari N. V., Cid Fernandes R., Stasińska G., Torres-Papaqui J. P., Mateus A., Sodré L., Schoenell W., Gomes J. M., 2007, MNRAS, 381, 263
Barton Gillespie E., Geller M. J., Kenyon S. J., 2003, ApJ, 582, 668
Barton E. J., Geller M. J., Kenyon S. J., 2000, ApJ, 530, 660
Bender R., Moellenhoff C., 1987, A&A, 177, 71
Bertola F., Bettoni D., Danziger J., Sadler E., Sparke L., de Zeeuw T., 1991, ApJ, 373, 369
Bresolin F., Gieren W., Kudritzki R.-P., Pietrzyński G., Urbaneja M. A., Carraro G., 2009, ApJ, 700, 309
Bruzual G., Charlot S., 2003, MNRAS, 344, 1000
Cardelli J. A., Clayton G. C., Mathis J. S., 1989, ApJ, 345, 245
Chabrier G., 2003, PASP, 115, 763
Cid Fernandes R., Gu Q., Melnick J., Terlevich E., Terlevich R., Kunth D., Rodrigues Lacerda R., Joguet B., 2004, MNRAS, 355, 273
Cid Fernandes R., Mateus A., Sodré L., Stasińska G., Gomes J. M., 2005, MNRAS, 358, 363
de Vaucouleurs G., de Vaucouleurs A., Corwin H. G., Jr, Buta R. J., Paturel G., Fouqué P., 1991, Third Reference Catalogue of Bright Galaxies. Volume III: Data for Galaxies between 12^h and 24^h. Springer, New York
Donzelli C. J., Pastoriza M. G., 1997, ApJS, 111, 181
Dors O. L., Jr, Copetti M. V. F., 2005, A&A, 437, 837
Dors O. L., Jr, Copetti M. V. F., 2006, A&A, 452, 473
Ellison S. L., Patton D. R., Simard L., McConnachie A. W., 2008, AJ, 135, 1877
Faber S. M., Gallagher J. S., 1979, ARA&A, 17, 135
Ferland G. J., 2002, Hazy, a Brief Introduction to Cloudy 96.03. Univ. Kentucky, Dept. Phys., Astron. internal report

Ferreiro D. L., Pastoriza M. G., 2004, A&A, 428, 837
Ferreiro D. L., Pastoriza M. G., Rickes M., 2008, A&A, 481, 645
Friedli D., Benz W., Kennicutt R., 1994, ApJ, 430, L105
Geller M. J., Kenyon S. J., Barton E. J., Jarrett T. H., Kewley L. J., 2006, AJ, 132, 2243
Hernquist L., 1993, ApJS, 86, 389
Howarth I. D., 1983, MNRAS, 203, 301
Hummer D. G., Storey P. J., 1987, MNRAS, 224, 801
Kennicutt R. C., Jr, Roettiger K. A., Keel W. C., van der Hulst J. M., Hummel E., 1987, AJ, 93, 1011
Kewley L. J., Ellison S. L., 2008, ApJ, 681, 1183
Kewley L. J., Geller M. J., Barton E. J., 2006, AJ, 131, 2004
Kewley L. J., Rupke D., Jabran Hahid H., Geller M. J., Barton E. J., 2010, ApJ, 721, L48
Krabbe A. C., Rembold S. B., Pastoriza M. G., 2007, MNRAS, 378, 569
Krabbe A. C., Pastoriza M. G., Winge C., Rodrigues I., Ferreiro D. L., 2008, MNRAS, 389, 1593
Lambas D. G., Tissera P. B., Alonso M. S., Coldwell G., 2003, MNRAS, 346, 1189
Leitherer C. et al., 1999, ApJS, 123, 3
MacArthur L. A., González J. J., Courteau S., 2009, MNRAS, 395, 28
McGaugh S. S., 1991, ApJ, 380, 140
Mateus A., Sodré L., Cid Fernandes R., Stasińska G., Schoenell W., Gomes J. M., 2006, MNRAS, 370, 721
Michel-Dansac L., Lambas D. G., Alonso M. S., Tissera P., 2008, MNRAS, 386, L82
Nikolic B., Cullen H., Alexander P., 2004, MNRAS, 355, 874
Peeples M. S., Pogge R. W., Stanek K. Z., 2009, ApJ, 695, 259
Roy J.-R., Walsh J. R., 1997, MNRAS, 288, 715
Rupke D. S. N., Veilleux S., Baker A. J., 2008, ApJ, 674, 172
Rupke D. S. N., Kewley L. J., Barnes J. E., 2010, ApJ, 710, L156
Schlegel D. J., Finkbeiner D. P., Davis M., 1998, ApJ, 500, 525
Sekiguchi K., Wolstencroft R. D., 1992, MNRAS, 255, 581
Sellwood J. A., Wilkinson A., 1993, Rep. Prog. Phys., 56, 173
Springel V., 2005, MNRAS, 364, 1105
Woods D. F., Geller M. J., 2007, AJ, 134, 527

This paper has been typeset from a TEX/LATEX file prepared by the author.